Int. J. Heat Mass Transfer. Vol. 36, No. 14, pp. 3515–3528, 1993
Printed in Great Britain

0017-9310/93 $6.00+0.00

CW laser machining of hard ceramics—I. Effects of three-dimensional conduction, variable properties and various laser parameters

SUBHRANSU ROY† and MICHAEL F. MODEST
Department of Mechanical Engineering, The Pennsylvania State University, University Park, PA 16802, U.S.A.

(*Received* 7 *July* 1992 *and in final form* 27 *January* 1993)

Abstract—A three-dimensional conduction model has been developed to predict the temperature distribution inside the solid and the shape of a groove formed by partial evaporation of a semi-infinite body using a moving CW laser with a Gaussian beam profile. This has application in laser machining where material is removed by repeated scanning of a focussed beam on the workpiece surface. The governing equations are solved using a finite-difference method on an algebraically-generated boundary-fitted coordinate system. The groove shape and temperature distribution in the solid for both constant properties and variable properties, for different speeds, for various laser power levels and for different beam profiles are presented. The groove shapes for constant thermal properties are compared with a previous three-dimensional boundary element conduction model solution and a quasi-one-dimensional conduction model solution, in which the conduction losses were approximated using a simple integral method. The present model compares well with the three-dimensional boundary element model for all ranges of laser parameters, and, when thermal losses due to conduction are minor, the one-dimensional results are also in good agreement. Experimental results were obtained for material removal rates and groove shapes on silicon nitride, which were found to agree well with theoretical predictions for shallow grooves. For deeper grooves in silicon nitride beam guiding (i.e. multiple reflections within the groove) comes into play and the assumptions in the model are violated.

1. INTRODUCTION

LASERS are routinely being used to produce holes, and for scribing and cutting thin sections of hard and brittle ceramics, but the application of lasers to machine ceramics into desired shapes by removing bulk material is relatively new. The feasibility of several machining operations based on overlapping of grooves, including turning, threading and milling has been demonstrated with some ceramics [1, 2]. It is clear from these works as well as the authors' own that a number of phenomena interact in the grooving process which are not well understood and, thus, make it impossible to predict the shape of single and overlapping grooves accurately. Theoretical as well as experimental investigations are necessary to understand the importance of various parameters that govern laser material interactions and influence the groove shape and size.

Most of the theoretical work on laser-processing heat transfer to date has centered on the solution of the classical heat conduction equation for a stationary or moving semi-infinite solid. Cases with and without phase change and for a variety of irradiation conditions have been studied and reviewed in a previous paper [3]. Although considerable theoretical research has been done on laser welding [4, 5] few theoretical studies have been done on laser cutting and scribing.

Laser scribing or shaping with a moving laser was modeled by Modest and Abakians [6] for irradiation by a CW laser with a Gaussian distribution onto an opaque semi-infinite solid. They assumed one-step evaporation of material (without beam interference), parallel laser beams, negligible reflection effects and small heat losses (in order to employ a simple integral method for conduction losses). Roy and Modest [3] relaxed one of the most restrictive assumptions made by Modest and Abakians [6] by including three-dimensional conduction effects, showing that a more accurate treatment of the conduction losses has a considerable effect on the size of the groove formed by evaporation, especially if scanning velocity is low (resulting in higher conduction losses). However, surface and bulk thermal properties were assumed constant in that study.

Recently, Ramanathan and Modest [7] modeled the situation of evaporative cutting for ceramics, including variable thermal properties. They found that variable property effects were relatively unimportant, even for such strong variation in properties as found in ceramics, provided that the constant property results were evaluated at evaporation temperature. They included conduction losses only normal to the surface and modeled the problem using a simple integral method. It was uncertain whether the weak depen-

†Present address: Center for Laser Technology, Indian Institute of Technology, Kanpur 208016, India.

NOMENCLATURE

B_1, B_2 constants
C_1, C_2, C_3 constants
c specific heat
F_0 radiation flux density at center of beam at focal plane
f functional variation of thermal diffusivity, $\alpha_H/\alpha_{H,ev}$
g functional variation of absorptivity, α/α_{ev}
h specific enthalpy
h_{rc} 'heat of removal'
$\mathbf{F}$ irradiation flux vector
$\hat{\mathbf{i}}, \hat{\mathbf{j}}, \hat{\mathbf{k}}$ unit vector in x, y and z directions
J Jacobian of transformation
k thermal conductivity
$\hat{\mathbf{n}}$ unit surface normal
N_e evaporation-to-laser power parameter
N_k conduction-to-laser power parameter
N_ξ, N_η, N_ζ number of grid points in ξ, η and ζ direction
$\mathbf{Q}$ dimensionless irradiation flux vector at surface, $\mathbf{F}/F_0$
$s(x, y)$ local groove depth
$S(x, y)$ dimensionless groove depth
$\bar{t}, t$ time, dimensionless time
T temperature
T_0 reference temperature
u laser scanning speed
U laser speed-to-diffusion parameter
w_0 $1/e^2$ radius of laser beam at focal plane
w local radius of laser beam
v_n transient surface recession normal to surface
$\bar{x}, \bar{y}, \bar{z}$ Cartesian coordinates
x, y, z dimensionless Cartesian coordinates.

Greek symbols
α_H thermal diffusivity
α local effective absorptivity at laser wavelength
β_{∞} far-field beam divergence angle
δ difference operator
θ dimensionless enthalpy
λ wavelength of laser radiation
ρ density of the medium
ξ, η, ζ dimensionless computational coordinates.

Subscripts
ev evaluated at evaporation (or decomposition) temperature
ξ, η, ζ derivative with respect to this variable
∞ evaluated at ambient conditions, or located far away.

dence of the predicted groove shape on the thermal properties was due to a deficiency in the integral model. In a follow-up paper Ramanathan and Modest [8] replaced the integral method with a more accurate finite-differencing scheme to account for one-dimensional conduction and variable thermal properties. The results showed considerable differences for variable properties, as compared to the results found in Ramanathan and Modest [7].

In the present paper a three-dimensional conduction model has been developed to predict the groove shapes and temperature field during evaporative scribing of a solid with variable properties, and subject to CW laser irradiation. The effect of machining parameters—laser power, scanning speed and beam profile are investigated. The boundary element formulation used in a previous paper [3] by the authors to solve the three-dimensional conduction equation for a moving body is unsuitable for variable properties within moving bodies, since this would require computation intensive volume integrations. Therefore, in the present paper the boundary element method is replaced by a finite-difference formulation with a boundary-fitted coordinate system. The transient form of the governing equation is used so that time-varying laser irradiation conditions can also be readily accommodated in future work. To validate the theoretical model, silicon nitride (Si_3Ni_4) was chosen as a typical ceramic material with its large variation of thermal properties. A 1500 W CO_2 laser was used to cut several grooves at various power levels and scanning speeds. Using available thermophysical properties data the material removal rates and groove shapes were computed and compared with experimental results.

2. THEORETICAL BACKGROUND

In order to obtain a realistic yet feasible description of the evaporation front in a moving solid subjected to a concentrated laser beam, the following simplifying assumptions will be made:

1. The solid moves with constant velocity u.
2. The solid is isotropic.
3. The density variation with temperature in a solid is negligible and therefore it is assumed constant in the conduction equation.
4. The material is opaque, i.e. the laser beam does not penetrate appreciably into the medium.
5. Change of phase from solid to vapor (or decomposition products) occurs in a single step at the evaporation (or decomposition) temperature T_{ev}. Real materials may display significantly different

behavior such as liquefaction followed by evaporation, decomposition into liquid and gas, gradual evaporation over a wide range of temperatures, outgassing followed by microexplosive removal of solid particles, etc. Assuming that the most important parameter is the total amount of energy required to remove material, referred to as 'heat of removal', the present model should do quite well.

6. The evaporated material does not interfere with the incoming laser beam and also ionization of the gas does not occur, which is true for most cutting and drilling applications at moderate power levels and in the presence of a gas jet. The size of the ejected particles and the condensed vapor, if any, above the workpiece is so small compared with the 10.6 μm laser wavelength that the absorption and scattering over the small beam travel length is insignificant. For cases where there is partial blockage of the beam by the ionized gas and ejected particles, the effects need to be lumped into the absorptivity parameter.

7. Heat losses by convection and radiation are negligible as compared to the intensity of the incident beam. These losses were shown not to affect the groove shape under all conditions [6].

8. Multiple reflections of laser radiation within the groove are neglected. This is a limitation which restricts the present model to shallow grooves or materials with high absorptivities (even at grazing angles), e.g. if the evaporation surface is rough. Multiple reflections of laser radiation within the groove are addressed in a companion paper [9].

Under these conditions the transient heat transfer equation for a solid (with constant density) moving with a velocity u in the positive $\bar{x}$-direction under a Gaussian laser beam (cf. Fig. 1) may be expressed in terms of specific enthalpy as:

$$\frac{\partial h}{\partial \bar{t}} + u\frac{\partial h}{\partial \bar{x}} = \nabla\cdot(\alpha_H \nabla h); \quad h = \int_{T_0}^{T} c\,\mathrm{d}T, \tag{1}$$

subject to the boundary conditions,

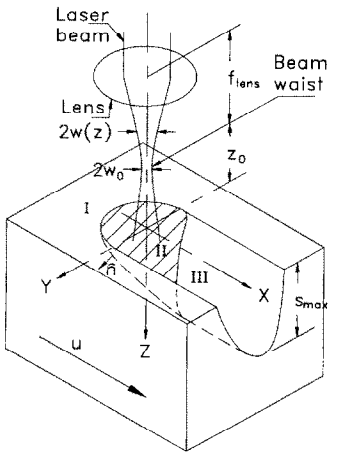

FIG. 1. Laser evaporation setup and coordinate system.

$$\bar{x}\to\pm\infty,\quad \bar{y}\to\pm\infty,\quad \bar{z}\to+\infty:\quad h = h_\infty, \tag{2a}$$

$$\bar{z} = s(\bar{x},\bar{y}):\ \alpha\mathbf{F}\cdot\hat{\mathbf{n}} = -\hat{\mathbf{n}}\cdot(\rho\alpha_H\nabla h) + (v_n - u\hat{\mathbf{i}}\cdot\hat{\mathbf{n}})\rho h_{re};$$

$$(v_n - u\hat{\mathbf{i}}\cdot\hat{\mathbf{n}})\rho h_{re} \geqslant 0 \tag{2b}$$

and an appropriate initial condition.

Boundary conditions (2b) state that the irradiation absorbed at the surface is used up by conduction losses into the solid and by evaporation, if present (if no evaporation takes place, i.e. during warm-up, cool-down and in regions too far away sideways from the laser beam, $v_n - u\hat{\mathbf{i}}\cdot\hat{\mathbf{n}} = 0$). At quasi-steady state, the transient recession in the direction normal to the surface (v_n) will become zero (i.e. the evaporation front will become stationary with respect to the laser), the temperature field in the solid will become steady in the frame of reference of the laser, and the energy expended for evaporation will be reduced to $-u\hat{\mathbf{i}}\cdot\hat{\mathbf{n}}\rho h_{re}$. Also, wherever evaporation takes place at steady state, $\hat{\mathbf{i}}\cdot\hat{\mathbf{n}} < 0$. In the present study, we are only interested in a quasi-steady solution.

The energy intensity distribution, $\mathbf{F}$, for a CW focussed Gaussian laser beam having a waist w_0 at the focal plane z_0 is given by Kogelnik and Li [10]:

$$\mathbf{F} = \left(\frac{w^2}{w_0^2}\right)^{-1} F_0\, e^{-2(\bar{x}^2+\bar{y}^2)/w^2(\bar{z})}\frac{\hat{\mathbf{s}}}{\hat{\mathbf{s}}\cdot\hat{\mathbf{k}}}, \tag{3a}$$

where

$$w^2(\bar{z}) = w_0^2 + \beta_\infty^2(\bar{z}-\bar{z}_0)^2, \tag{3b}$$

defines the beam radius, w, away from focus and

$$\beta_\infty = \frac{\lambda}{\pi w_0} \tag{3c}$$

is the far-field beam divergence angle for the diffraction limited case of a Gaussian beam. Also, $F_0 = 2P/\pi w_0^2$ is the flux at the center of a Gaussian beam at the focal plane, P is the total laser power, w_0 is the $1/e^2$-radius of the focal spot containing 86.5% of the beam's energy. If the laser beam is visualized as consisting of a bundle of rays having direction $\hat{\mathbf{s}}(\bar{x},\bar{y},\bar{z})$, perpendicular to the wave-front of propagation, then $\hat{\mathbf{s}}$ can be related to the radius of the wave-front [11], $\bar{r}_c(z)$, as:

$$\frac{\hat{\mathbf{s}}}{\hat{\mathbf{s}}\cdot\hat{\mathbf{k}}} = \frac{\bar{x}\hat{\mathbf{i}}+\bar{y}\hat{\mathbf{j}}}{\sqrt{(\bar{r}_c^2(\bar{z})-\bar{x}^2-\bar{y}^2)}} + \hat{\mathbf{k}}, \tag{4a}$$

$$\bar{r}_c(z) = (\bar{z}-\bar{z}_0)\left[1+\frac{w_0^2/\beta_\infty^2}{(\bar{z}-\bar{z}_0)^2}\right]. \tag{4b}$$

The boundary conditions (2) are sufficient to solve equation (1) for the enthalpy if the groove shape s is already established and v_n is zero. However, since the groove shape is to be determined, two more conditions are needed:

$$\bar{z} = s(\bar{x},\bar{y}):\quad h(\bar{x},\bar{y}) = h_{re},\quad \text{if}\quad (v_n - u\hat{\mathbf{i}}\cdot\hat{\mathbf{n}}) > 0 \tag{5a}$$

and

$$s(-\infty, \bar{y}) = 0. \quad (5b)$$

Equation (5a) states that during evaporation (i.e. when $v_n - u\hat{\mathbf{i}}\cdot\hat{\mathbf{n}} > 0$) the surface is at evaporation temperature.

To non-dimensionalize the governing equations and boundary conditions the following non-dimensional variables and parameters are introduced:

$$x = \sqrt{2}\bar{x}/w_0;\ y = \sqrt{2}\bar{y}/w_0;\ z = \sqrt{2}\bar{z}/w_0;\ s = \sqrt{2}\bar{s}/w_0$$

$$t = 2\alpha_{H,ev}\bar{t}/w_0^2;\ f = \alpha_H/\alpha_{H,ev};\ g = \alpha/\alpha_{ev};$$

$$\theta = \frac{h-h_s}{h_{ev}-h_s} = \frac{\int_{T_s}^{T} c\,dT}{\int_{T_s}^{T_{ev}} c\,dT};\ U = \frac{uw_0}{\alpha_{H,ev}\sqrt{2}};\ V_n = \frac{v_n w_0}{\alpha_{H,ev}\sqrt{2}};$$

$$N_k = \frac{\sqrt{2}\rho\alpha_{H,ev}(h_{ev}-h_s)}{\alpha_{ev}F_0 w_0};\ N_e = \frac{u\rho h_{re}}{\alpha_{ev}F_0};\ \mathbf{Q} = \frac{\mathbf{F}}{F_0}. \quad (6)$$

Physically, N_e gives the ratio of power required to evaporate material normal to the irradiation, and the absorbed laser flux; N_k approximates the ratio of conduction losses, again for a surface normal to irradiation, and the absorbed laser flux; U relates the laser scanning speed to that of thermal diffusion into the medium, and V_n represents a similar non-dimensional transient recession of the evaporating surface with respect to the laser. The functions f and g describe the variable thermal diffusivity and absorptivity, respectively. The factor $\sqrt{2}$ appears in some of the dimensionless groups because $w_0/\sqrt{2}$, the 1/e-radius of a Gaussian beam, has been chosen as a characteristic length scale in order to be consistent with the previous works of the authors.

The non-dimensional form of the governing equation then follows as:

$$\frac{\partial\theta}{\partial t} + U\frac{\partial\theta}{\partial x} = \nabla\cdot(f\nabla\theta) \quad (7)$$

and the boundary condition equations become:

$$z \to \pm\infty,\quad y \to \pm\infty,\quad z \to +\infty:\quad \theta = 0; \quad (8)$$

$$z = S(x, y):\ g\mathbf{Q}\cdot\hat{\mathbf{n}} = -N_k f\hat{\mathbf{n}}\cdot\nabla\theta + (V_n - U\hat{\mathbf{i}}\cdot\hat{\mathbf{n}})\frac{N_e}{U};$$

$$(V_n - U\hat{\mathbf{i}}\cdot\hat{\mathbf{n}})\frac{N_e}{U} \geqslant 0 \quad (9a)$$

$$\theta = 1, \quad \text{if} \quad V_n - U\hat{\mathbf{i}}\cdot\hat{\mathbf{n}} > 0, \quad \text{and} \quad S(-\infty, y) = 0. \quad (9b)$$

Equation (7) with its boundary conditions (8) and (9) form a complete set of dimensionless equations in transient form for the solution of the groove shape $S(x, y)$ and enthalpy field $\theta(x, y, z)$. This set of equations is similar to the one used by the authors in a previous BEM solution [3] except that the definition of the dimensionless terms have been modified to accommodate variable properties, and transient terms are included.

3. SOLUTION APPROACH

The governing equations with non-linear boundary conditions applied to a complex groove geometry are solved using finite-difference techniques with a boundary-fitted coordinate system. The body-conforming coordinate system simplifies the application of boundary conditions, and nodal points are clustered in regions of rapid change to improve solution accuracy.

3.1. *Coordinate transformation*

Explicit relations to map the physical domain, (x, y, z), to a uniformly spaced rectangular coordinate region, (ξ, η, ζ), will be described later. Symbolically, the functional relations are:

$$x = x(\xi, \eta, \zeta, \tau), \quad y = y(\xi, \eta, \zeta, \tau),$$
$$z = z(\xi, \eta, \zeta, \tau), \quad t = \tau;$$
$$\xi = \xi(x, y, z, t), \quad \eta = \eta(x, y, z, t),$$
$$\zeta = \zeta(x, y, z, t), \quad \tau = t. \quad (10)$$

The functional form of the metric quantities ($\xi_x = \partial\xi/\partial x$, $\xi_y = \partial\xi/\partial y$, $\xi_z = \partial\xi/\partial z$, etc.), required to transform an equation from a physical coordinate system to computational coordinates has been given by Anderson *et al.* [12], and is repeated here for convenience:

$$\frac{\partial(x, y, z)}{\partial(\xi, \eta, \zeta)} = 1/J = x_\xi(y_\eta z_\zeta - y_\zeta z_\eta) + x_\eta(y_\zeta z_\xi - y_\xi z_\zeta) + x_\zeta(y_\xi z_\eta - y_\eta z_\xi), \quad (11a)$$

$$\begin{bmatrix} \xi_x & \xi_y & \xi_z \\ \eta_x & \eta_y & \eta_z \\ \zeta_x & \zeta_y & \zeta_z \end{bmatrix} = J\begin{bmatrix} (y_\eta z_\zeta - y_\zeta z_\eta) & (-x_\eta z_\zeta + x_\zeta z_\eta) & (x_\eta y_\zeta - x_\zeta y_\eta) \\ (y_\zeta z_\xi - y_\xi z_\zeta) & (-x_\xi z_\zeta + x_\xi z_\zeta) & (x_\zeta y_\xi - x_\xi y_\zeta) \\ (y_\xi z_\eta - y_\eta z_\xi) & (-x_\xi z_\eta + x_\eta z_\xi) & (x_\xi y_\eta - x_\eta y_\xi) \end{bmatrix}, \quad (11b)$$

$$\xi_t = -x_\tau\xi_x - y_\tau\xi_y - z_\tau\xi_z;\ \eta_t = -x_\tau\eta_x - y_\tau\eta_y - z_\tau\eta_z;$$
$$\zeta_t = -x_\tau\zeta_x - y_\tau\zeta_y - z_\tau\zeta_z. \quad (11c)$$

The mapping functions (10) need not be known analytically; the partial derivatives x_ξ, x_η, x_ζ are computed using central difference formulas and then the metric quantities can be obtained. The following abbreviations are also defined for later use:

$$A^{\xi\xi} = \nabla\xi\cdot\nabla\xi \quad A^{\eta\eta} = \nabla\eta\cdot\nabla\eta \quad A^{\zeta\zeta} = \nabla\zeta\cdot\nabla\zeta$$
$$A^{\xi\eta} = \nabla\xi\cdot\nabla\eta \quad A^{\xi\zeta} = \nabla\xi\cdot\nabla\zeta \quad A^{\eta\zeta} = \nabla\eta\cdot\nabla\zeta. \quad (12)$$

3.2. *Grid generation*

Corresponding to the physical space (x, y, z) a well ordered rectangular computation domain (ξ, η, ζ) is set up with uniform grid spacing of $\Delta\xi = \Delta\eta = \Delta\zeta = 1$. The present study is limited to the case where the absorbed irradiation is symmetric about the center plane resulting in a symmetric groove. Therefore, the grid is constructed on one side of the center plane. In Fig. 2 the computational domain (ξ, η, ζ), which is a rectangular parallelepiped is shown alongside the physical domain (x, y, z) bounded by curved surfaces.

The computational coordinate system is constructed with $N_\xi \times N_\eta \times N_\zeta$ nodal points in the region bounded by the irradiated surface ($\zeta = 1$) and another surface ($\zeta = N_\zeta$), far into the body not heated by the laser. Unidirectional interpolation (in the ζ-direction, in this case) using Hermite polynomials is used between each grid point (ξ, η) on the boundary, $\zeta = 1$, and the corresponding point (ξ, η) on the opposite boundary, $\zeta = N_\zeta$ [13, 14]. Since the Hermite interpolation functions are third-order polynomials, two more conditions, i.e. continuity of the slopes of the ζ-line at the two boundaries, are enforced. To simplify the interpolation the ζ-coordinate (interpolation direction) is replaced by a scaled coordinate v such that $0 < v < 1$. The interpolation scheme is defined by:

$$\mathbf{r}(\xi, \eta, v) = F_1(v)\mathbf{r}(\xi, \eta, 0) + F_1(1-v)\mathbf{r}(\xi, \eta, 1) + F_2(v)\mathbf{r}_v(\xi, \eta, 0) - F_2(1-v)\mathbf{r}_v(\xi, \eta, 1); \quad (13)$$

$$F_1(v) = (1-v)^2(1+2v), \quad F_2(v) = (1-v)^2 v, \quad (14)$$

where $\mathbf{r}$ is the position vector,

$$\mathbf{r}(\xi, \eta, v) = x(\xi, \eta, v)\hat{\mathbf{i}} + y(\xi, \eta, v)\hat{\mathbf{j}} + z(\xi, \eta, v)\hat{\mathbf{k}}. \quad (15)$$

The out-of-surface directional derivatives are chosen carefully as:

$$\mathbf{r}_v(\xi, \eta, 0) = C_1|\mathbf{r}(\xi, \eta, 1) - \mathbf{r}(\xi, \eta, 0)|\hat{\mathbf{l}}(\xi, \eta, 0);$$

$$\hat{\mathbf{l}}(\xi, \eta, 0) = \frac{\nabla\zeta}{|\nabla\zeta|}; \quad (16a)$$

$$\mathbf{r}_v(\xi, \eta, 1) = C_2|\mathbf{r}(\xi, \eta, 1) - \mathbf{r}(\xi, \eta, 0)|\hat{\mathbf{l}}(\xi, \eta, 1);$$

$$\hat{\mathbf{l}}(\xi, \eta, 1) = \hat{\mathbf{k}}. \quad (16b)$$

The magnitudes of the directional derivatives $\mathbf{r}_v$ are represented as C_1 or C_2 times the distance from point $(\xi, \eta, 0)$ to $(\xi, \eta, 1)$. While $\mathbf{r}_v(\xi, \eta, 0)$ is perpendicular to the irradiated surface, $\zeta = 1$, making the grid orthogonal locally, $\mathbf{r}_v(\xi, \eta, 1)$ was chosen to be in the direction of $\hat{\mathbf{k}}$. C_1 and C_2 must be less than 3 to avoid loops and kinks in the v-line joining points $(\xi, \eta, 0)$ and $(\xi, \eta, 1)$. C_1 and C_2 were chosen to be 0.3 and 1.5, respectively, to ensure a smooth grid system under all conditions. The nodes are spaced equally along the ζ-line in the computational coordinate, but in physical space the nodes are clustered near the irradiated boundary $v = 0$ (i.e. $\zeta = 1$) by introducing a stretching parameter, $C_3 = \{1.05\text{–}1.1\}$, with the nodal locations $v(\zeta)$ found as the roots of

$$F_1(1-v) + C_1F_2(v) - C_2F_2(1-v) = \frac{C_3^{(\zeta-1)} - 1}{C_3^{(N_\zeta-1)} - 1};$$

$$\zeta = \{1 \ldots N_\zeta\} \quad \text{and} \quad 0 < v < 1. \quad (17)$$

The v-coordinate is only used for the purpose of grid generation and is again replaced by ζ in the subsequent development of the equations.

Equations (13)–(17) uniquely assign a physical coordinate (x, y, z) to each point in the computational space having coordinates $(\xi = 1 \ldots N_\xi)$, $(\eta = 1 \ldots N_\eta)$ and $(\zeta = 1 \ldots N_\zeta)$.

3.3. *Transformed equations*

The governing equation is transformed to the rectangular computational coordinate region. The non-conservative form of the transformed equation is lengthy but can be easily derived as [15]:

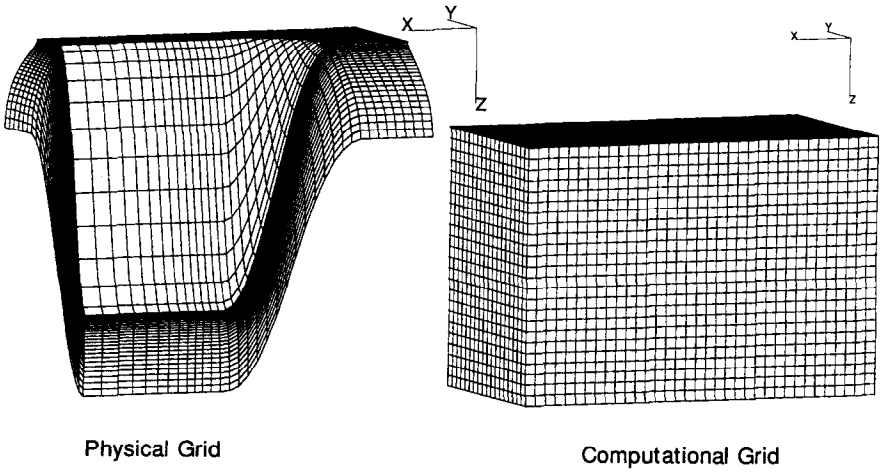

FIG. 2. Physical and computational grid system.

$$\theta_\tau+(\xi_t+U\xi_x)\theta_\xi+(\eta_t+U\eta_x)\theta_\eta+(\zeta_t+U\zeta_x)\theta_\zeta$$
$$=A^{\xi\xi}(f\theta_\xi)_\xi+A^{\eta\eta}(f\theta_\eta)_\eta+A^{\zeta\zeta}(f\theta_\zeta)_\zeta$$
$$+A^{\xi\eta}[(f\theta_\eta)_\xi+(f\theta_\xi)_\eta]+A^{\xi\zeta}[(f\theta_\zeta)_\xi+(f\theta_\xi)_\zeta]$$
$$+A^{\eta\zeta}[(f\theta_\zeta)_\eta+(f\theta_\eta)_\zeta]$$
$$+f(\nabla^2\xi\theta_\xi+\nabla^2\eta\theta_\eta+\nabla^2\zeta\theta_\zeta), \tag{18}$$

where

$$\nabla^2\xi=-\nabla\xi\cdot\mathbf{D},\quad \nabla^2\eta=-\nabla\eta\cdot\mathbf{D},$$
$$\nabla^2\zeta=-\nabla\zeta\cdot\mathbf{D}, \tag{19a}$$
$$\mathbf{D}=D^x\hat{\mathbf{i}}+D^y\hat{\mathbf{j}}+\mathbf{D}^z\hat{\mathbf{k}};$$

$$D^x=A^{\xi\xi}x_{\xi\xi}+A^{\eta\eta}x_{\eta\eta}+A^{\zeta\zeta}x_{\zeta\zeta}$$
$$+A^{\xi\eta}2x_{\xi\eta}+A^{\xi\zeta}2x_{\xi\zeta}+A^{\eta\zeta}2x_{\eta\zeta}, \tag{19b}$$

$$D^y=A^{\xi\xi}y_{\xi\xi}+A^{\eta\eta}y_{\eta\eta}+A^{\zeta\zeta}y_{\zeta\zeta}$$
$$+A^{\xi\eta}2y_{\xi\eta}+A^{\xi\zeta}2y_{\xi\zeta}+A^{\eta\zeta}2y_{\eta\zeta}, \tag{19c}$$

$$D^z=A^{\xi\xi}z_{\xi\xi}+A^{\eta\eta}z_{\eta\eta}+A^{\zeta\zeta}z_{\zeta\zeta}$$
$$+A^{\xi\eta}2z_{\xi\eta}+A^{\xi\zeta}2z_{\xi\zeta}+A^{\eta\zeta}2z_{\eta\zeta}. \tag{19d}$$

The boundary conditions are also transformed to computational coordinates:

Irradiated surface, $\zeta=1$:

$$g\mathbf{Q}\cdot\nabla\zeta=-N_k[f(A^{\xi\zeta}\theta_\xi+A^{\eta\zeta}\theta_\eta+A^{\zeta\zeta}\theta_\zeta)]$$
$$-(\zeta_t+U\zeta_x)\frac{N_e}{U};\quad (\zeta_t+U\zeta_x)\frac{N_e}{U}\leqslant 0 \tag{20}$$

$$\theta=1,\quad \text{if}\quad (\zeta_t+U\zeta_x)<0 \tag{21}$$

Far upstream,

$$\xi=1:\theta=0 \tag{22}$$

Far sideways,

$$\eta=N_\eta:\theta=0 \tag{23}$$

Far bottom,

$$\zeta=N_\zeta:\theta=0 \tag{24}$$

Far downstream,

$$\xi=N_\xi:\theta_x=\xi_x\theta_\xi+\eta_x\theta_\eta+\zeta_x\theta_\zeta=0 \tag{25}$$

In the center plane,

$$\eta=1:\theta_y=\xi_y\theta_\xi+\eta_y\theta_\eta+\zeta_y\theta_\zeta=0. \tag{26}$$

Equation (25) is used instead of a constant ambient temperature boundary condition, $\theta=0$, as the nodal system is truncated at a finite distance downstream of the laser heating zone. However, the boundary surface, $\xi=N_\xi$, is constructed far enough from the evaporating groove surface such that θ is negligible.

Although we are interested in a steady state solution, the equations required to solve for θ will be used in the transient form so that a time-iterative solution procedure can be adopted. The non-linear boundary condition (20) and equation (21) are coupled and need to be solved simultaneously to get the transient surface recession velocity, ζ_t, so that the groove surface can be updated in a time-marching fashion. An easier alternative approach to arrive at the quasi-steady state solution is to use equation (20) to calculate the temperature and use the following equation to update the surface depth:

$$\Delta S=\text{sgn}\,(\theta-1)B_1\,e^{-B_2|\theta-1|}\quad\text{if}\quad \zeta_x<0; \tag{27}$$

$$\zeta_x<0\Leftrightarrow\hat{\mathbf{i}}\cdot\hat{\mathbf{n}}<0,\quad\text{where}\quad \hat{\mathbf{n}}=\frac{\nabla\zeta}{|\nabla\zeta|}.$$

The constants B_1 and B_2 are chosen suitably to achieve convergence. While this procedure will not give the correct transient groove depth and enthalpy, the solution will finally converge to equation (21) at quasi-steady state when $\Delta S=0$ and $\zeta_t=0$.

4. COMPUTATIONAL PROCEDURE

The transformed equation (18) in θ is finite-differenced and solved using an approximate factorization (ADI-type) algorithm (Anderson *et al.* [12]). The second-order accurate finite-difference for first, second and mixed derivatives are represented as:

$$\delta_\xi(\theta)_{i,j,k}=\tfrac{1}{2}(\theta_{i+1,j,k}-\theta_{i-1,j,k}), \tag{28a}$$

$$\delta_\xi[f\delta_\xi(\theta)]_{i,j,k}=\tfrac{1}{2}[(f_{i+1,j,k}+f_{i,j,k})(\theta_{i+1,j,k}-\theta_{i,j,k})$$
$$-(f_{i,j,k}+f_{i-1,j,k})(\theta_{i,j,k}-\theta_{i-1,j,k})], \tag{28b}$$

$$\delta_\eta[f\delta_\xi(\theta)]_{i,j,k}=\tfrac{1}{4}[f_{i,j+1,k}(\theta_{i+1,j+1,k}-\theta_{i-1,j+1,k})$$
$$-f_{i,j-1,k}(\theta_{i+1,j-1,k}-\theta_{i-1,j-1,k})], \tag{28c}$$

where i,j,k represent grid point indices and $\delta_\xi,\delta_\eta,\delta_\zeta$ represent finite-differencing in ξ,η,ζ directions respectively.

At the boundary points where, at most, first-order partials must be represented, a second-order accurate one-sided difference was used to approximate θ_ζ. The second-order formula appropriate for the boundary point $(i,j,1)$ on the surface $\zeta=1$ is:

$$\delta_\zeta(\theta)_{i,j,1}=\tfrac{1}{2}(-\theta_{i,j,3}+4\theta_{i,j,2}-3\theta_{i,j,1}). \tag{29}$$

Second-order differencing must be used at the groove boundary, $\zeta=1$, because the temperature change can be very high into the body over the nodes even though the nodes are placed closely. However, one-sided differencing of the coordinate values in the ζ-direction, e.g. x_ζ, need only be first-order accurate because the nodes are closely spaced.

The governing equation is then represented in difference form as:

$$\frac{\theta^{n+1}-\theta^n}{\Delta\tau}=\mathscr{L}^\xi(\theta^{n+1})+\mathscr{L}^\eta(\theta^{n+1})$$
$$+\mathscr{L}^\zeta(\theta^{n+1})+\mathscr{L}^0(\theta^n) \tag{30}$$

where n is the iteration level, and the difference operators $\mathscr{L}$ at internal nodes are defined as:

$$\mathscr{L}^{\xi}(\theta) = A^{\xi\xi}\delta_{\xi}\{f\delta_{\xi}\theta\} - (\xi_t + U\xi_x)\delta_{\xi}(\theta),$$
$$\mathscr{L}^{\eta}(\theta) = A^{\eta\eta}\delta_{\eta}\{f\delta_{\eta}\theta\} - (\eta_t + U\eta_x)\delta_{\eta}(\theta),$$
$$\mathscr{L}^{\zeta}(\theta) = A^{\zeta\zeta}\delta_{\zeta}\{f\delta_{\zeta}\theta\} - (\zeta_t + U\zeta_x)\delta_{\zeta}(\theta) \quad (31a)$$

$$\mathscr{L}^{0}(\theta) = A^{\xi\eta}[\delta_{\xi}\{f\delta_{\eta}(\theta)\} + \delta_{\eta}\{f\delta_{\xi}(\theta)\}] + A^{\xi\zeta}[\delta_{\xi}\{f\delta_{\zeta}(\theta)\} + \delta_{\zeta}\{f\delta_{\xi}(\theta)\}] + A^{\eta\zeta}[\delta_{\eta}\{f\delta_{\zeta}(\theta)\} + \delta_{\zeta}\{f\delta_{\eta}(\theta)\}] + f[\delta_{\xi}(\theta)\nabla^2\xi + \delta_{\eta}(\theta)\nabla^2\eta + \delta_{\zeta}(\theta)\nabla^2\zeta]. \quad (31b)$$

Expressing θ in incremental-form, $\theta^{n+1} = \theta^n + \Delta\theta$, and since $\mathscr{L}^{\xi}(\theta+\Delta\theta) = \mathscr{L}^{\xi}(\theta) + \mathscr{L}^{\xi}(\Delta\theta)$, we get:

$$(1-\Delta\tau\mathscr{L}^{\xi})(1-\Delta\tau\mathscr{L}^{\eta})(1-\Delta\tau\mathscr{L}^{\zeta})(\Delta\theta) = \Delta\tau\mathscr{R}(\theta^n), \quad (32a)$$

where

$$\mathscr{R}(\theta^n) = \mathscr{L}^{\xi}(\theta^n) + \mathscr{L}^{\eta}(\theta^n) + \mathscr{L}^{\zeta}(\theta^n) + \mathscr{L}^{0}(\theta^n), \quad (32b)$$

which is the same as equation (30) if the higher-order terms of order $\Delta\tau^2$ are neglected, since the time step $\Delta\tau$ is small. At steady state, when $\Delta\theta = 0$, equation (32) reduces to $\mathscr{R}(\theta) = 0$. Note that all cross-derivitives have been shifted to the right-hand side of equation (32) to allow straightforward matrix inversion. The above equation in three space variables is split into three equations each containing one space variable. The approximate factorization algorithm (ADI-type) is thus implemented in three steps:

$$(1-\Delta\tau\mathscr{L}^{\xi})\Delta\theta^{*} = \Delta\tau\mathscr{R}(\theta^n), \quad (33a)$$
$$(1-\Delta\tau\mathscr{L}^{\eta})\Delta\theta^{**} = \Delta\theta^{*}, \quad (33b)$$
$$(1-\Delta\tau\mathscr{L}^{\zeta})\Delta\theta = \Delta\theta^{**}, \quad (33c)$$
$$\theta^{n+1} = \theta^n + \Delta\theta. \quad (33d)$$

The difference operators, $\mathscr{L}^{\xi}$, $\mathscr{L}^{\eta}$, $\mathscr{L}^{\zeta}$, each give rise to tridiagonal matrices when the algebraic difference equations at all grid points are collected. The algorithm, therefore, requires a series of scalar, tridiagonal inversions and can be implemented efficiently.

A first approximation of s (i.e. the groove shape) is obtained using a simple integral method by neglecting conduction parallel to the surface (quasi-one-dimensional model); this makes the equations governing groove depth first-order hyperbolic and, thus, they can be solved with a simple forward stepping technique [6]. For known values of s new values of absorbed flux $\mathbf{Q}$ are calculated; then equations (33) are solved along with the boundary condition equations to get the enthalpy θ. Wherever $\theta > 1$, the value of s is increased and wherever $\theta < 1$ while $\hat{\mathbf{i}}\cdot\hat{\mathbf{n}} < 0$, s is decreased until the groove depth converges to a steady value. The incremental (or decremental) value for s is estimated using equation (27).

5. NUMERICAL VALIDATION

To compare the results from the three-dimensional conduction model with the one-dimensional model, three different sets of parameter values were chosen. While N_c was kept constant at 0.1, N_k values of 0.05, 0.01, and 0.002 were used. The scanning velocity U was chosen such that $U \times N_k = 0.1$, which ensures a constant rate of energy deposition. Figure 3(a) shows the development of the groove centerline for these cases and Fig. 3(b) shows the fully-developed groove profile using the one-dimensional conduction model, the present three-dimensional conduction model and a three-dimensional boundary element model [3]. For large values of the conduction parameter N_k the groove depth predicted by the three-dimensional conduction model is smaller than that predicted by the one-dimensional model, since the one-dimensional conduction model underestimates conduction losses by neglecting sideways conduction. As N_k is reduced to 0.002 and the scanning velocity U is increased to 50 the conduction losses become insignificant compared to the energy deposition and the three-dimensional groove profile prediction matches that of the one-dimensional groove profile. From Fig. 3(a) it is noted that the three-dimensional and one-dimensional conduction model predictions are very close for negative x locations (i.e. when the groove has just started forming), even at the centerline, because of small conduction losses. The present model agrees well with the three-dimensional boundary element model results for all ranges of laser parameters.

6. MATERIAL PROPERTY EVALUATION

To predict groove size for specific ceramic materials, thermophysical properties are needed to solve the equations described earlier. The ceramic material considered in this study is hot-pressed silicon nitride (Si_3N_4). The evaluation of the properties for silicon nitride has been described extensively by Ramanathan and Modest [7] and is briefly discussed here. The properties used in this study are given in Table 1.

Figure 4(a) shows thermal diffusivity data bands for some types of silicon nitride based ceramics [16]. Such a large drop in thermal diffusivity with temperature is common for many ceramic materials. The low temperature thermal diffusivity (and conductivity) is affected by porosity, phase content, and free silicon content. Hot-pressed (HP) silicon nitride generally has higher conductivity than reaction-sintered (RS) silicon nitride due to higher density and also varies little at high temperatures. The thermal diffusivity data used here are the same as those of Wallace [17] which was extended to the decomposition temperature through curve fitting by Ramanathan and Modest [7]. Curve-fits were done on the

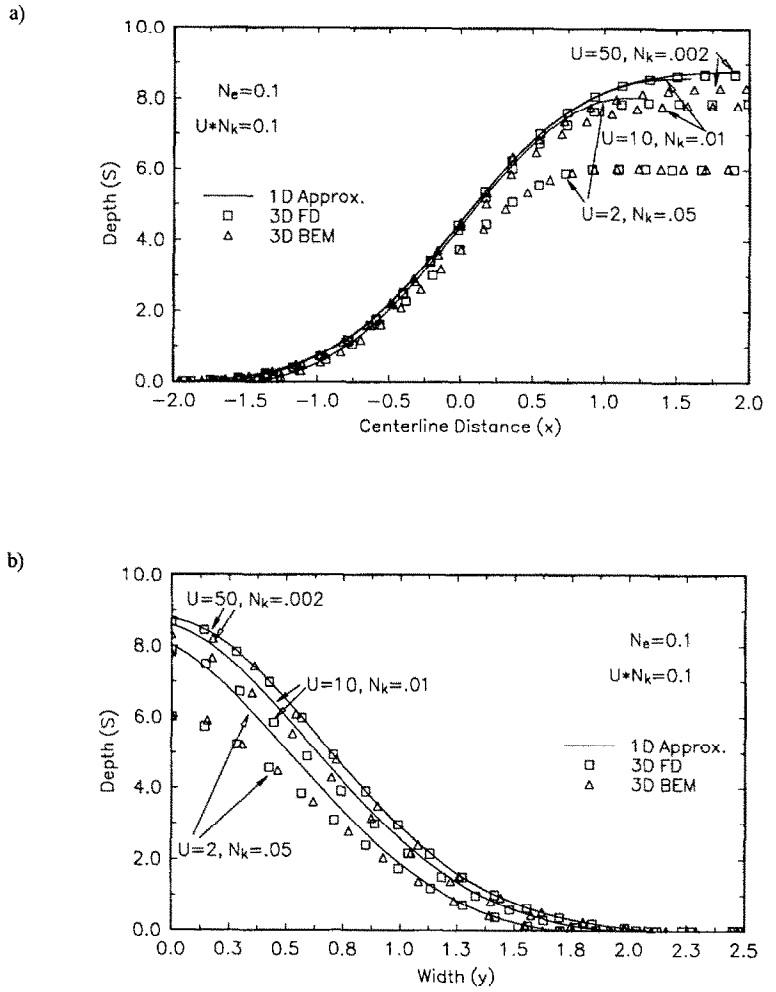

FIG. 3. Comparison of 1-D and 3-D results. (a) Groove development along centerline. (b) Fully developed groove cross-section.

thermal conductivity and thermal diffusivity data separately.

The specific heat of silicon nitride increases twofold as the temperature is raised from room temperature to decomposition temperature. However, it is a volumetric property and does not vary as much with impurities and micro-structure as thermal diffusivity or thermal conductivity. The specific heat data are the same as those of Wallace [17] which were curve-fitted by Ramanathan and Modest [7].

The heat of removal for Si_3N_4 was calculated based on the following decomposition reaction given by Singhal [18] and others, which state that silicon nitride decomposes into liquid silicon and gaseous nitrogen:

$$Si_3N_4(s) \rightarrow 3Si(l) + 2N_2(g).$$

Wallace and Copley [1] and Yamamoto and Yamamoto [19] also concluded that liquid silicon is formed during cutting of silicon nitride with a CO_2 laser. Wallace and Copely explained that above a temperature of 2151 K the production of subsurface nitrogen at a pressure greater than 0.1 MPa causes the silicon liquid layer to rupture and be ejected. The JANAF tables [20] were used to calculate the enthalpy change during the above reaction at 2151 K. The enthalpy values for temperatures up to 2400 K were also calculated for comparison and were found to vary insignificantly over this temperature range. The heat of removal would change considerably if the silicon is evaporated at the atmospheric boiling temperature of 3500 K. It was assumed that such high temperatures are not reached and the enthalpy

Table 1. Material properties for Si_3N_4

T_{ev}	2151 K	h_{re}	6206 kJ kg^{-1}
c_{ev}	1294.5 J kg^{-1} K^{-1}	α_{ev}	0.15
k_{ev}	12.14 W m^{-1} K^{-1}	α	0.23, $\theta < 1$
ρ	3250 kg m^{-3}	c/c_{ev}	$1.007\,(1-e^{-T/427})$
		k/k_{ev}	$1642/T+0.24$

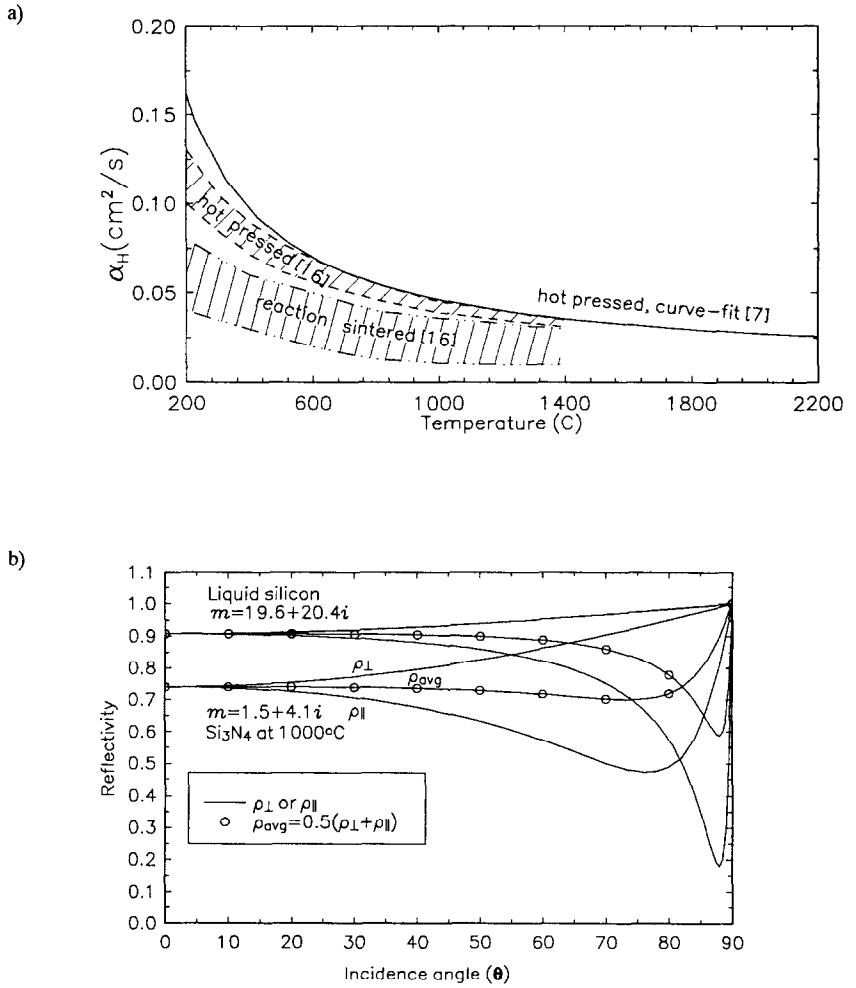

FIG. 4. Thermophysical properties of silicon nitride. (a) Thermal diffusivity of solid. (b) Reflectivity of solid and liquid phase.

required to decompose silicon nitride at 2151 K into liquid silicon and gaseous nitrogen was used in the calculations.

The absorptivity in the evaporation zone was estimated by assuming that the surface where the decomposition takes place is at least partially covered with a thin layer of liquid silicon (a product of the decomposition reaction). The reflectivity of molten silicon at the CO_2 laser wavelength, calculated from its complex refractive index ($m = 19.6 - 20.4i$) [21, 22], is shown alongside the reflectivity of solid silicon nitride at 1000°C and 10.6 μm [23] in Fig. 4(b). The absorptive index, k, for liquid silicon is so high that even a thin film of liquid silicon (say, 1 μm) is optically opaque, and, therefore, the reflectivity of the interface between the liquid silicon film and the solid silicon nitride need not be accounted for. Absorptivities of solid silicon nitride were measured at various temperatures [23]. Based on these measurements an average absorptivity of 0.23 was used for the solid silicon nitride surface which has not undergone decomposition, and an average absorptivity of 0.15 was used for the evaporating surface. Since the decomposition-front surface is expected to be only partially covered with a liquid silicon film through which nitrogen is escaping, the actual local absorptivity should be in the range $0.1 < \alpha < 0.3$ (based on extrapolating the absorptivity of solid silicon nitride to be approximately 0.3 near the decomposition temperature).

7. COMPARISON BETWEEN EXPERIMENTAL AND THEORETICAL RESULTS

To determine the range of applicability of the model as applied to laser grooving of real ceramic materials, several grooves were made on silicon nitride ceramic for different power levels (600, 1100 and 1500 W) and different scanning speeds (5, 10 and 20 cm s^{-1}). The samples were sectioned in half with a diamond blade perpendicular to the scanning direction. Scanning electron microscope (SEM) pictures of the groove cross-sections on the two exposed surfaces were digi-

tized resulting in two sets of groove cross-section data for each groove. The experimental grooves were then compared with those predicted by theory. The experiments were performed with a 1500 W, fast axial flow CO_2 laser, model Everlase S51, manufactured by Coherent General. The setup consisted of a beam delivery system that contains a focusing ZnSe lens and a coaxial gas nozzle for assist gas, all housed in a beam delivery pipe. The beam exiting from the laser cavity is linearly polarized and a circular polarizer was used to convert the beam to a circularly polarized one. The workpiece was mounted on a computer-controlled workstation, model MT160, manufactured by Klinger Scientific, that can be moved in the $\bar{x}$- and $\bar{y}$-directions at predetermined speeds. The beam width is difficult to measure accurately at focus. A 86.5%-energy beam radius of 212 μm at focus gave reasonably good agreement between calculated and experimentally observed groove width for silicon nitride over a range of powers and speeds. This theoretical estimate of the beam radius was checked by measuring the intensity profile of the expanded beam away from the focus with a traversing thermocouple. The divergence of a beam away from the waist is related to the beam width at focus by a beam quality factor, M^2, whose minimum value is 1 for the diffraction limited divergence of a pure TEM_{00} mode Gaussian beam. For a non-Gaussian higher-order beam, the beam expansion follows the hyperbolic relation [24]

$$w^2(\bar{z}) = w_0^2 + \beta_\infty^2 (\bar{z} - \bar{z}_0)^2; \quad \beta_\infty = M^2 \frac{\lambda}{\pi w_0}.$$

The beam radius, w, was measured as 6.27 mm at a distance of 128 mm away from focus. This corresponds to a focussed beam waist of 212 μm for an M^2 value of 3.1. Such an M^2 value lies within the range of values specified by the manufacturer for this type of laser [25]. The intensity profile also appeared smooth and 'Gaussian-like' although it is known to contain some higher order non-Gaussian modes. For calculation purposes the intensity profile was assumed to be Gaussian. It was noted that the width of the beam varies by only 5% at a distance of 1000 μm away from focus even for an M^2 of 3.8 which can be considered to be an upper limit for these types of lasers. As the grooves were cut with the beam focussed on the surface of the sample and were shallower than 1000 μm, the beam width was assumed constant and the direction of the laser rays were assumed to be in the direction of $\hat{\mathbf{k}}$, i.e. $\hat{\mathbf{s}} = \hat{\mathbf{k}}$.

To ensure that the quality of the beam exiting from the nozzle is constant, all the experimental results presented here were obtained during a single time period in a single lot without disturbing the beam delivery setup. A thorough statistical analysis of the experimental error has not been done at this time. However, it can be said that measuring the groove outline from the SEM pictures is difficult and subjective and may be the source for large errors. This is particularly true for deep grooves, if redeposition of evaporated and ejected material occurs. For deep grooves the error in groove depth measurement using SEM pictures is estimated to be as high as $\pm 5\%$ and for shallow grooves approximately $\pm 3\%$. The overall experimental uncertainty due to non-repeatibility of processing conditions may be higher.

The volume removal rates for silicon nitride obtained from the experiments are compared with calculated values for effective absorptivity values (in the ablation zone) of 0.15 and 0.20 in Fig. 5(a). These estimates were made for the case of constant properties with the thermal diffusivity and specific heat evaluated at the decomposition temperature. It was observed experimentally that there is a distinct rise in material removal rate at lower speeds while the theoretically calculated variation in material removal rates over the range of speeds is relatively small at any given power. The experimentally observed rise is even more pronounced at higher powers. Apparently, such increase in material removal rate at lower speeds is due to better coupling between the laser and the groove surface : as the groove becomes deeper, beam trapping due to multiple reflections inside the groove increases the effective absorption. From the graph it is seen that at lower powers and shallow grooves the decomposition zone absorptivity appears to be about 15%. At such low powers the grooves are shallow and beam trapping due to diffuse reflections is very small and beam trapping due to specular reflections is non-existent. However, at higher powers and slow speeds the effective absorptivity could be as high as 25% for the data shown. How much of that is due to specular reflections and how much is due to diffuse reflections is not known. This issue is discussed in a separate companion paper [9].

If variable properties are accounted for (Fig. 5(b)) it is observed that the theoretically calculated material removal rates drop by 5–15%, the decrease being more pronounced at lower speeds. This is the result of two opposing effects. As the temperature decreases away from the evaporation zone the thermal conductivity increases resulting in higher overall conduction losses and less material removal rate. On the other hand, since the heat capacity is lower at temperatures below evaporation temperature, less heat is required to heat up the material.

During the laser grooving process only a portion of the laser energy is used to raise the temperature of the removed material (sensible heat) and decompose the material (latent heat). The rest is conducted into the workpiece only to heat up the material below the decomposition temperature and does not directly contribute to removal of material. The approximate theoretical estimate of heat losses are 43, 29, and 25% of the absorbed power at beam power levels of 600, 1100 and 1500 W respectively. The above theoretical estimate was made considering that 15% of the beam power is absorbed and the thermophysical properties are constant. Since the heat penetration depth is small,

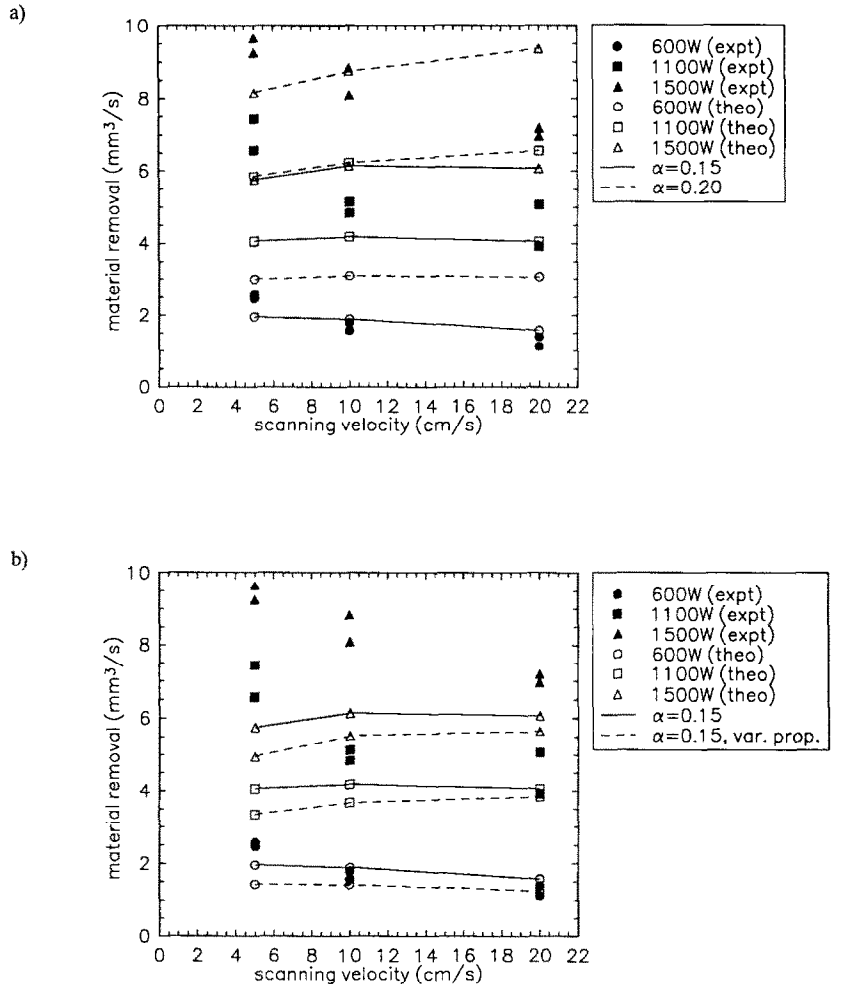

FIG. 5. Material removal rates during laser grooving. (a) Considering constant properties. (b) Considering variable properties.

much of the heat that is conducted into the workpiece is eventually utilized to decompose material. At higher powers the removal process becomes more efficient.

While examination of material removal rates gives an overall idea of the removal process from a heat transfer point of view, the shape of the grooves as predicted by theory and observed in experiments gives additional insight into the material removal process. Figure 6 shows the influence of two different beam profiles on theoretical predictions of groove shape and material removal rates assuming constant thermophysical properties, comparing a Gaussian profile and another flatter beam profile having the same power (1100 W) and 86.5%-radius. Reduction in the peak power of the beam results in a more even distribution of the laser energy, which in turn produces a wider groove bottom as shown in Fig. 6(b). The groove depth is reduced by 10% for the flatter beam profile but material removal rate is increased by 3%.

All experimental grooves (cf. Fig. 7) are wide and well rounded at the bottom. For shallow grooves (i.e. all grooves cut at 20 cm s^{-1} and also the 600 W groove cut at 10 cm s^{-1}) the theoretical predictions of groove shape are very close to actual grooves. For such shallow grooves the depth of the heat-affected zone is relatively large (due to lower groove surface area and higher energy deposition per unit area) and side-ways heat conduction makes the grooves wide at the bottom. For deeper grooves at 1100 and 1500 W (cf. Fig. 7) the predicted shapes (for a Gaussian beam and without internal reflections) are somewhat less wide at the bottom. For such deep grooves the redistribution of the absorbed laser energy due to internal reflections apparently deepens and widens the groove as evident from the experimental data, and is addressed in a companion paper [9].

Hard ceramics are brittle and prone to breakage due to thermal shock. Under certain conditions of temperature and speed unfavorable temperature profiles and high cooling rates at the downstream end may cause undesirable stress conditions leading to material breakage. Although analyzing thermal stress

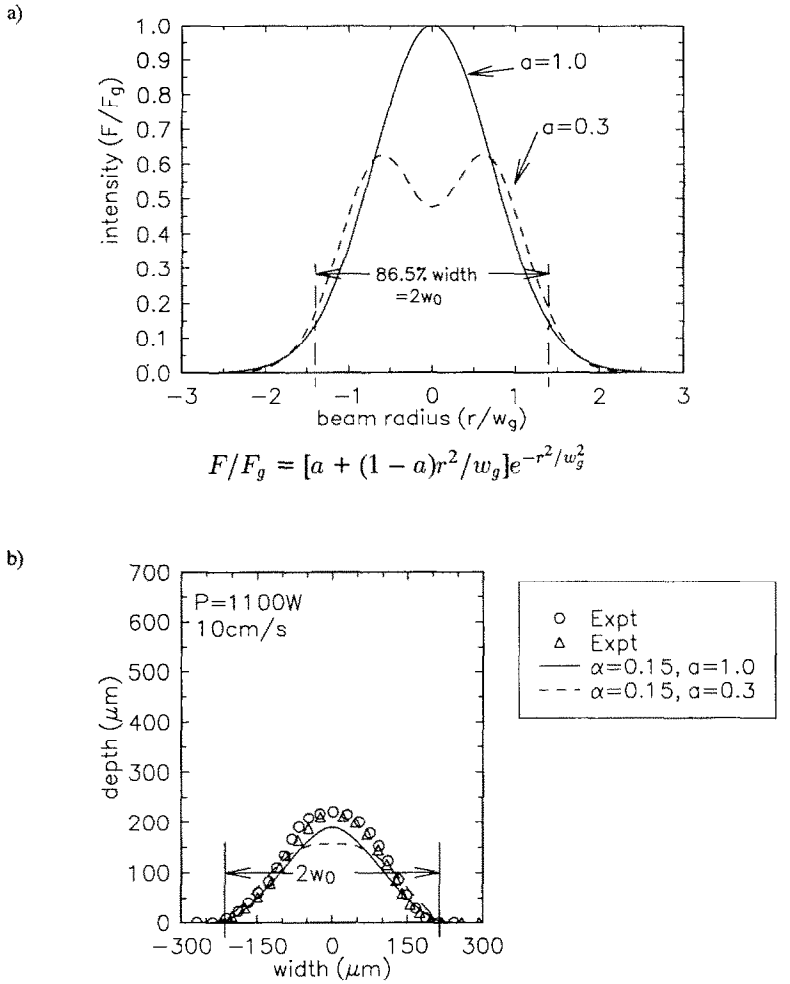

FIG. 6. Effect of beam profile on groove shape. (a) Two beam profiles—Gaussian ($a = 1.0$ or TEM_{00}) and non-Gaussian ($a = 0.3$ or $0.3\,TEM_{00} + 0.7\,TEM_{01^*}$). (b) Groove shapes corresponding to the beam profiles.

is not within the scope of this work a qualitative investigation into the temperature profiles was performed. Knowing temperature profiles also gives a theoretical estimate of the heat affected zone. Figure 8 shows the temperature profiles in the plane of symmetry for grooves cut at 1500 W and speeds of 5 and 20 cm s^{-1}, calculated using temperature-dependent properties. It is observed that the temperature drops at a slightly lower rate into the medium at slower scanning speeds. For the present set of cutting parameters the temperature drops by 50% over a distance of about 50–75 μm into the bulk material (i.e. 25–30% of the beam radius). On the other hand, the cooling rate (i.e. temperature decay in the x-direction) at the trailing region is higher at slower scanning speeds.

8. CONCLUSIONS

In this study we have modeled the problem of evaporative cutting of a material with a moving CW laser. The effect of process parameters—laser power, scanning speed and beam profile—were presented. Theoretical predictions of groove size were made using the properties of hot-pressed silicon nitride and were compared with experimental results. An estimate of the three-dimensional conduction losses revealed that heat loss by conduction can be between 25 and 45% of the absorbed laser power, the losses being lower at the highest power of 1500 W. If variable properties are considered (instead of constant values evaluated at the evaporation or decomposition temperature) the material removal rate drops by 5–15%. For shallow grooves, the agreement between theoretically predicted and experimentally measured material removal rates and groove shapes for silicon nitride were within the bounds of experimental uncertainty. For deep grooves (high laser power and/or slow scanning speeds) the present model underpredicts the groove depth, since multiple reflections must be accounted for, especially if the material has a high reflectivity.

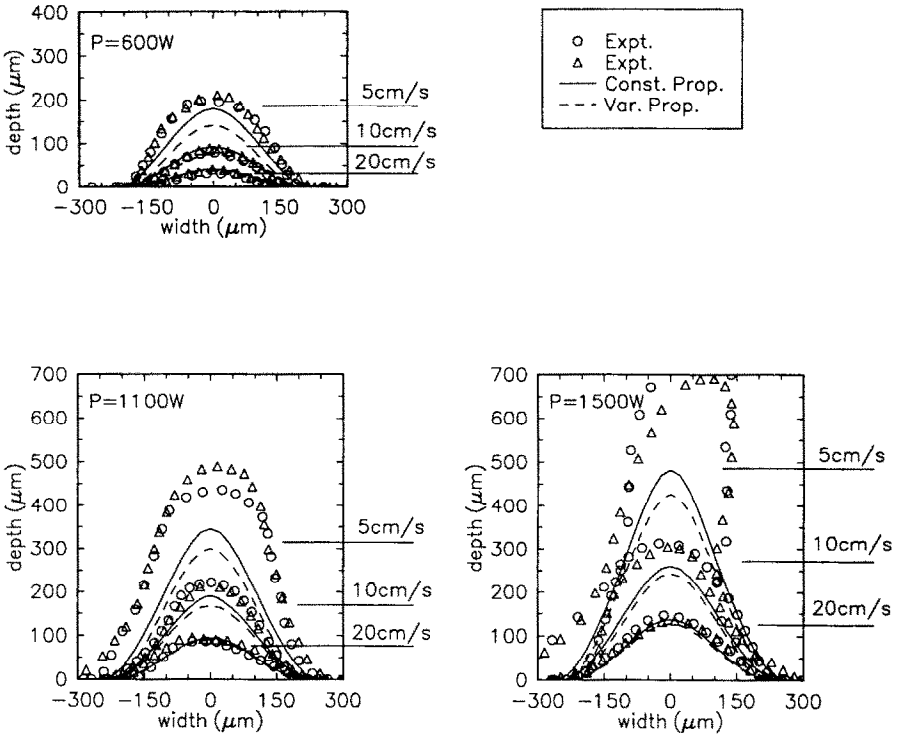

FIG. 7. Groove cross-section at different scanning speeds and power levels of 600, 1100 and 1500 W.

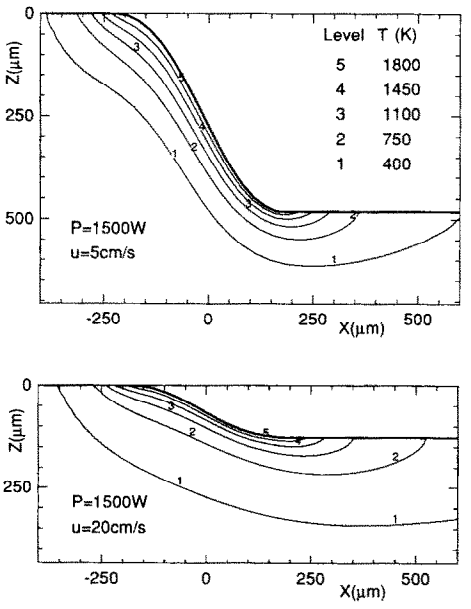

FIG. 8. Temperature profile in the plane of symmetry at 1500 W power and scanning speed 20 cm s^{-1} and 5 cm s^{-1}.

Acknowledgements—Support for this work by National Science Foundation Grant CTS-8915027 is gratefully acknowledged. The authors would like to thank Dr S. Ramanathan for measuring the beam profile.

REFERENCES

1. R. J. Wallace and S. M. Copley, Laser machining of silicon nitride: energetics, *Adv. Ceramic Mater.* **1**(3), 277–283 (1986).
2. G. Chryssolouris and J. Bredt, Machining of ceramics using a laser lathe, *Int. Ceramics Rev.* 70–72 (April 1988).
3. S. Roy and M. F. Modest, Three-dimensional conduction effects during evaporative scribing with a CW laser, *J. Thermophys. Heat Transfer* **4**(2), 199–203 (1990).
4. J. Mazumder and W. M. Steen, Heat transfer model for CW laser material processing, *J. Appl. Phys.* **51**(2), 941–947 (1980).
5. T. Chande and J. Mazumder, Estimating effects of processing conditions and variable properties upon pool shape, cooling rates, and absorption coefficient in laser welding, *J. Appl. Phys.* **56**(7), 1981–1986 (1984).
6. M. F. Modest and H. Abakians, Evaporative cutting of a semi-infinite body with a moving CW laser, *J. Heat Transfer* **108**, 602–607 (1986).
7. S. Ramanathan and M. F. Modest, Effect of variable properties on evaporative cutting with a moving CW laser. In *Heat Transfer in Space Systems*, Vol. HTD-135, ASME (1990).
8. S. Ramanathan and M. F. Modest, Single and multiple pass cutting of ceramics with a moving CW laser. In *Proceedings of the XXII ICHMT Intl. Symposium on Manufacturing and Materials Processing*, Dubrovnik, Yugoslavia (1990).
9. S. Y. Bang, S. Roy and M. F. Modest, CW laser machining of hard ceramics—II. Effects of multiple reflections, *Int. J. Heat Mass Transfer* **36**, 3529–3540 (1993).
10. H. Kogelnik and T. Li, Laser beams and resonators, *Appl. Optics* **5**(10), 1550–1565 (1956).

11. J. T. Luxon and D. E. Parker, *Industrial Lasers and Their Applications* (1st Edn). Prentice-Hall, Englewood Cliffs, NJ (1985).
12. D. A. Anderson, J. C. Tannehill and R. H. Pletcher, *Computational Fluid Mechanics and Heat Transfer*. Hemisphere, New York (1984).
13. P. E. Eiseman, A multi-surface method of coordinate generation, *J. Comp. Phys.* **33**, 118–150 (1979).
14. L. Eriksson, Three-dimensional spline-generated coordinate transformations for grids around wing-body configurations. In *Numerical Grid Generation Techniques*, Hampton, Virginia, pp. 253–264, NASA Conference Publication 2166 (1980).
15. J. F. Thompson, Z. U. Warsi and C. W. Mastin, *Numerical Grid Generation, Foundations and Applications*. North-Holland, New York (1985).
16. D. C. Larsen, J. W. Adams and R. Ruh, The nature of SiC for use in heat engines as compared to Si_3N_4: an overview of property differences. In *Progress in Nitrogen Ceramics*, Vol. 65 of *NATO ASI Series E: Applied Sciences*, Netherlands, pp. 695–710 (1983).
17. R. J. Wallace, A study of the shaping of hot pressed silicon nitride with a high power CO_2 laser, Ph.D. Thesis, University of Southern California, Los Angeles, CA (1983).
18. S. C. Singhal, Thermodynamic analysis of the high-temperature stability of silicon nitride and silicon carbide, *Ceramurgia Int.* **2**, 123–130 (1976).
19. J. Yamamoto and Y. Yamamoto, Laser machining of silicon nitride. In *International Conference on Laser Advanced Materials Processing—Science and Applications*, Osaka, Japan, pp. 297–302, High Temperature Society of Japan, Japan Laser Processing Society (1987).
20. D. R. Stull and H. Prophet, *JANAF Thermochemical Tables*, Dept. of Commerce, NBS, Washington, D.C. (1971).
21. C. P. Grigoropoulos, Inhomogeneous melting of thin silicon films irradiated with CO_2 laser light, Paper No. 91-HT-40 (July 1991).
22. J. R. Preston, J. E. Sipe and H. E. Van Driel, Phase diagram of laser induced melt morphologies on silicon. In *Materials Research Society Symposia Proceedings*, Vol. 51, Pittsburg, Pennsylvania, pp. 137–142, Materials Research Society (1986).
23. S. Roy, S. Y. Bang, M. F. Modest and V. S. Stubican, Measurement of spectral, directional reflectivities of solids at high temperatures between 9 and 11 μm. In *Proceedings of the Third ASME/JSME Thermal Engineering Joint Conference*, Vol. 4 (1991), also *Appl. Optics* (in press) (1993).
24. A. E. Siegman, New developments in laser resonators. In *Optical Resonators, Proceedings of LASE '90*, Los Angeles, 16–18 January 1990, SPIE–The International Society for Optical Engineering (1990).
25. Personal communication with Mr K. D. Hachfeld, Coherent General.